Topological nodal line states in three-dimensional ball-and-stick sonic crystals

Zhi-Guo Geng,[1] Yu-Gui Peng,[1] Ya-Xi Shen,[1] Zhen Ma,[1] Rui Yu,[2,*] Jin-Hua Gao,[1] and Xue-Feng Zhu[1,†]

[1]*School of Physics and Innovation Institute, Huazhong University of Science and Technology, Wuhan, Hubei 430074, People's Republic of China*

[2]*School of Physics and Technology, Wuhan University, Wuhan, Hubei 430072, People's Republic of China*

(Received 11 July 2019; revised manuscript received 30 November 2019; published 18 December 2019)

Nodal line states in electronic systems are the extended band crossings in three-dimensional (3D) momentum space, which recently has been widely explored in classical systems in analogs. With the Dirac cones in two-dimensional (2D) hexagonal lattices, the linear degeneracy points in the stacking 2D hexagonal lattices (3D lattices) are elongated into degeneracy lines in the momentum space. In this work, we show that by coupling the stacked hexagonal lattices with the time-reversal symmetry and inversion symmetry protected, degeneracy points will form a closed nodal ring in the momentum space in the strong coupling regime. We observe flat drumhead dispersion surfaces in the band gaps, which verifies the existence of the intriguing nodal line states. Based on full-wave simulations, we show the field confinement at the truncated surface and the field enhancement due to the large density of states in flat bands. Furthermore, topological robustness of the drumhead surface states is investigated against various randomly distributed defects, such as site disorders and hopping disorders. Our work may serve as the platform of the sonic-crystal based semimetal for versatile applications like sound trapping, vibration isolation, and absorption.

DOI: 10.1103/PhysRevB.100.224105

I. INTRODUCTION

Topological nontrivial phases have attracted considerable interests in various systems [1,2] for their novel physics, such as the notable quantum Hall effect [3,4] and quantum spin-Hall effect [5,6]. In the past decade, the paradigm of topological phase transition in electronic systems has been successfully shifted to classical systems [7,8] to bring forward the optical and acoustic analogs of the Chern insulators [9–12], spin-Hall-like topological insulators [13–17], and valley-Hall-like topological insulators [18–21]. Recently, the gapless topological phases, firstly discovered in semimetals [22–28] where the conduction and valence bands coincide at robust degenerate points (either discrete points [23–26] or continuum lines [22,27,28]), have also motivated widespread attention in optics [29–35] and acoustics [36–48]. For example, the Weyl sonic crystals featured with the robust one-way surface states have been experimentally realized in chiral artificial structures with broken inversion symmetries [37,38]. Different from the Weyl sonic crystals that require the protection of translation lattice symmetry, the nodal line sonic crystals with full line degeneracies require an additional protection of the crystalline symmetries [49]. The previous nodal line semimetals can be categorized into three groups either in electronic systems or in classical systems: (1) the lattices with the mirror reflection symmetry [32,41,50,51]; (2) the lattices with the time-reversal and inversion symmetries [52–56]; and (3) the lattices with the nonsymmorphic symmetry [33,34,39,57].

Acoustic wave, as the intrinsic longitudinal wave without complex interactions to the propagation medium, can be regarded as a good candidate to explore the properties of the nodal line states. In this work, we show that the three-dimensional (3D) ball-and-stick sonic crystals with both the time-reversal and inversion symmetry can have closed nodal lines (or nodal rings) in the momentum space. When the nodal ring is projected onto the Brillouin-zone surface, one can map out the drumhead surface states according to the bulk-boundary correspondence. Here the flat nodal lines are distinctly isolated from the bulk bands, where the surface localized states can be easily excited at the degenerate frequency. The proposed ball-and-stick sonic crystal is also a good candidate for the tight-binding model, where the effective Hamiltonian is derived to show the nontrivial properties of nodal rings and drumhead surface states. Finally, we impose different randomly distributed defects in the 3D lattice, such as site disorders, intralayer- and interlayer hopping disorders, which verifies the robustness of drumhead states against weak-strength perturbations. Our work will push forward the exploration of acoustic nodal line semimetals.

This work is organized as follows. In Sec. II, we study the nodal line states and the Weyl states in 3D momentum space of the ball-and-stick sonic crystal. A tight-binding model is introduced to derive the effective Hamiltonian and analyze the requirements for the dispersionless nodal rings. In Sec. III, we show the properties of the propagating Tamm-like states and the localized nodal line states (or the drumhead surface states), and reveal their inherent differences. In addition, different randomly distributed bulk disorders are introduced in the nodal line sonic crystals to verify the stability of the surface localized states under topological protection. We also investigate the cases of intrinsic and nonintrinsic source excitations

*yurui@whu.edu.cn
†xfzhu@hust.edu.cn

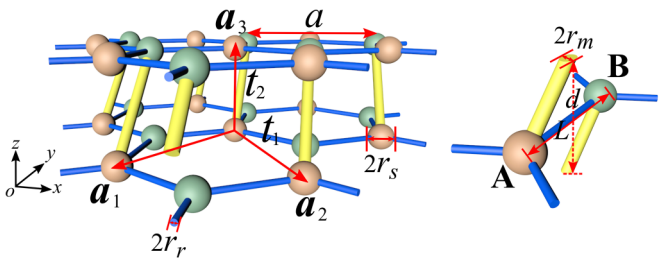

FIG. 1. A side view of one layer of the ball-and-stick sonic crystal. The hollow-sphere cavities and cylindrical channels are assembled into an acoustic network that is filled with air (density 1.25 kg/m^3 and speed of sound 340 m/s). The right panel shows an enlarged unit cell with the structural parameters marked. The cavities **A** and **B** locate at inequivalent lattice sites. The blue and yellow channels represent intralayer and interlayer acoustic couplers with the coupling strengths denoted by t_1 and t_2, respectively. Lattice vectors are $\boldsymbol{a}_1$, $\boldsymbol{a}_2$, and $\boldsymbol{a}_3$.

in the nodal line sonic crystals. Finally, we summarize the results in Sec. IV.

II. MODEL AND THEORY

A. Three-dimensional ball-and-stick sonic crystals

To achieve symmetry-protected nodal lines, we propose a toy model as shown in Fig. 1. The model is a multilayered structure stacking along the z direction. In each layer, we have two triangular sublattices with the lattice constant a. Note that no spin degree of freedom is considered in this model. In Fig. 1, the orange ball **A** and green ball **B** locate at different lattice sites. The blue and yellow sticks connect the balls **A** and **B** in each layer and between adjacent layers, respectively. The projection of the slanted yellow sticks is along the y direction of the x-y plane. Basically, the intralayer and interlayer couplings are not necessarily the same. The right panel of Fig. 1 shows a unit cell of the 3D lattice, where there exists an inversion symmetry between the two inequivalent sublattices. For acoustic implementation, the balls and sticks are replaced by hollow-sphere cavities and cylindrical channels. The network is filled with air for sound propagation. For the structural parameters, the spacing between two adjacent cavities **A** and **B** in plane is $L = 10$ cm. The in-plane and out-of-plane lattice constants are $a = 17.32$ cm and $d = 10$ cm. Since we set the equal length of L and d, the tilted angle of the interlayer pipes is 45°. The radii of the sphere cavities and in-plane pipes are $r_s = 1.5$ cm and $r_r = 0.3$ cm, respectively. In this work, the radius of out-of-plane pipes can be tailored to change the interlayer coupling strength.

The hexagonal lattice is a two-dimensional (2D) structure featured with the Dirac cones in the 2D momentum space [58]. By stacking the hexagonal lattices into a 3D structure, it is intuitive to consider the existence of degenerate nodal lines in the 3D momentum space. We first discuss a simple case in which the stacked hexagonal lattices are not coupled with each other. In this case, the band-crossing points will form straight nodal lines along the k_z direction in the 3D Brillouin

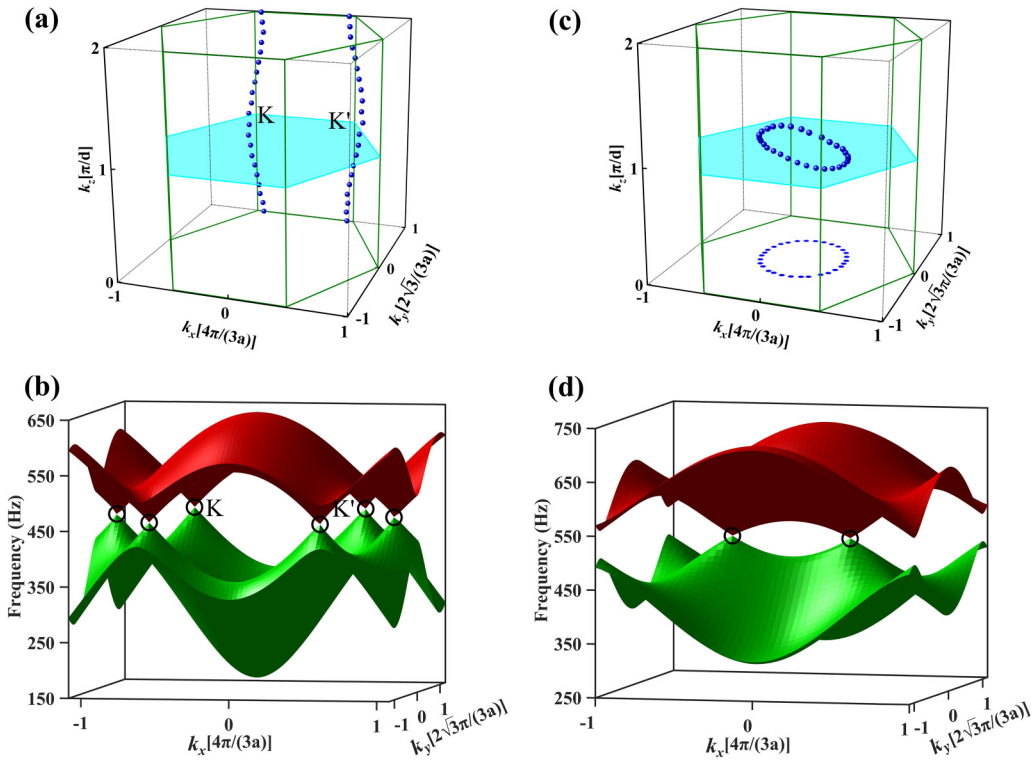

FIG. 2. (a) A series of band-crossing points on a pair of twisted nodal lines in the 3D Brillouin zone in presence of the weak interlayer coupling. The plane at $k_z = \pi/d$ is highlighted. (b) The band structure in the 2D Brillouin zone at $k_z = \pi/d$. The six band-crossing points (or nodal points) are marked by the black circles. (c) A closed nodal ring in the 3D Brillouin zone in presence of the strong interlayer coupling. (d) The band structure in the 2D Brillouin zone at $k_z = \pi/d$. The two nodal points are shifted inwardly by the strong interlayer interaction.

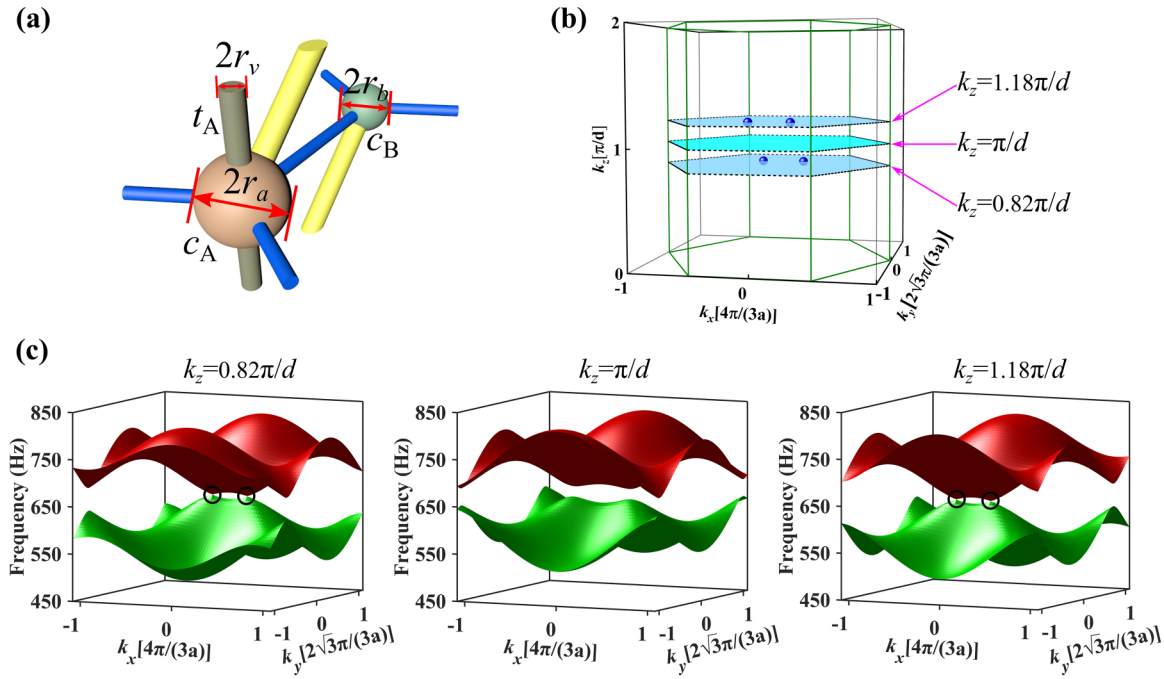

FIG. 3. (a) A schematic of the unit cell with broken inversion symmetry. The on-site energies c_A and c_B are different, and the interlayer hopping strengths between A-A and B-B sites $t_A \neq t_B$, with $t_B = 0$ in this model. (b) The 3D Brillouin zone of the inversion symmetry broken lattice. The four spheres label the Weyl points. (c) The band structures in the 2D Brillouin zone at $k_z = 0.82\pi/d$, $k_z = \pi/d$, $k_z = 1.18\pi/d$, as highlighted by the planes in (b). A pair of band-crossing points exist at $k_z = 0.82\pi/d$ and $k_z = 1.18\pi/d$, respectively.

zone, which is physically equivalent to the 2D system. As shown in Fig. 1, we can use the slanted pipes to introduce interlayer interactions without breaking the lattice inversion symmetry. In Fig. 2, we show the shape of nodal lines in the weak- and strong interlayer couplings, respectively. When the interlayer coupling strength is smaller than that of the intralayer coupling (for example, $r_m = 0.18$ cm and $r_r = 0.3$ cm), the acoustic system operates in the weak-coupling regime. In this case, the band-crossing point is slightly pushed away from the K and K' points. As shown in Fig. 2(a), the band-crossing points cover all k_z values, denoted by the blue spheres, which form the nodal lines twisted around the edge of the 3D hexagonal Brillouin zone. Here we only show two nodal lines in the vicinity of the K and K' points, since the Brillouin zone is periodic. It should be pointed out that the nodal line states are dispersionless, that is, the same frequency for all band-crossing points. In Fig. 2(b), we calculate the two lowest bands at $k_z = \pi/d$, where there exist six Dirac cones nearby the high-symmetric corners of the Brillouin zone, with the Dirac points locating at around 464 Hz, as marked by the black circles. In contrast to weak coupling, strong coupling is generated by enlarging the cross section of interlayer slanted pipes to ensure that the interlayer coupling strength weighs more than that of the intralayer coupling. In this work, we choose $r_m = 0.55$ cm and $r_r = 0.3$ cm. Affected by the strong interlayer interaction, the nodal lines are heavily deformed and warped into a closed ring, as shown in Fig. 2(c). The results show that the enhanced interlayer hopping strength makes the band-crossing points k_z dependent and far from the high-symmetric points in the 3D Brillouin zone. The closed nodal ring is centered at the point $(0, 0, \frac{\pi}{d})$ in the momentum space and tilted a little away from the $k_z = \pi/d$ plane, which is protected by the time-reversal and inversion symmetries without involving the spin-orbital coupling. It needs to be mentioned that the nodal ring will locate right in the $k_z = \pi/d$ plane, if we further introduce the mirror symmetry along the z direction into the 3D lattice. We can project the bulk nodal ring onto the bottom surface (001) of the Brillouin zone, where the associated surface Brillouin zone is divided into the outside topological nontrivial region (π Zak phase) and inside trivial region (0 Zak phase), as will be discussed in the next section. The closed nodal ring is also dispersionless. In Fig. 2(d), we calculate the band structure at $k_z = \pi/d$ and identify two band-crossing points at the degeneracy frequency of 530 Hz.

As aforementioned, the combination of time-reversal symmetry and inversion symmetry protects the nodal ring in the 3D momentum space. Therefore, it is expected that the nodal ring will gap out and may turn into discrete Weyl points after breaking the inversion symmetry [29,56]. As an example, we connect sphere cavities at A-A sites in adjacent layers with an air channel (the brown stick, radius: $r_v = 0.49$ cm). In Fig. 3(a), t_A represents the interlayer hopping strength between A-A sites. c_A and c_B are the on-site energies at A and B sites, respectively. The radii of sphere cavities at A and B sites are $r_a = 2$ cm and $r_b = 1.2$ cm, which are different to introduce an inversion-symmetry breaking into the 3D sonic crystal. With the breaking of inversion symmetry, gaps are opened along the nodal ring, except the Weyl points. As shown in Fig. 3(b), there exist four Weyl points in the 3D Brillouin zone at $k_z = 0.82\pi/d$ and $k_z = 1.18\pi/d$. Figure 3(c) further presents the band structures in the 2D Brillouin zone at $k_z = 0.82\pi/d$, $k_z = \pi/d$, and $k_z = 1.18\pi/d$, which identifies a pair of band-crossing points at $k_z = 0.82\pi/d$ and

$k_z = 1.18\pi/d$, respectively. At other k_z, such as $k_z = \pi/d$, the nodal ring fully gaps out.

B. The tight-binding model

The effective Hamiltonian for the nodal line states is derived as follows. For each 2D hexagonal lattice layer, the translation vectors are

$$\boldsymbol{a}_1 = \frac{a}{2}(1, \sqrt{3}),\ \boldsymbol{a}_2 = \frac{a}{2}(-1, \sqrt{3}), \tag{1}$$

where a is the in-plane lattice constant. From the lattice vectors, we obtain the corresponding reciprocal lattice vectors

$$\boldsymbol{b}_1 = \frac{2\pi}{a}\left(1, \frac{\sqrt{3}}{3}\right),\ \boldsymbol{b}_2 = \frac{2\pi}{a}\left(-1, \frac{\sqrt{3}}{3}\right). \tag{2}$$

Using these Bloch basis vectors, we will arrive at the effective Hamiltonian in the following [56,58]:

$$H_{\text{eff}}(\boldsymbol{k}) = \begin{pmatrix} 0 & -t_1 - t_1 e^{i\boldsymbol{k}\cdot(\boldsymbol{a}_2-\boldsymbol{a}_1)} - t_1 e^{-i\boldsymbol{k}\cdot\boldsymbol{a}_1} \\ -t_1 - t_1 e^{i\boldsymbol{k}\cdot(\boldsymbol{a}_1-\boldsymbol{a}_2)} - t_1 e^{i\boldsymbol{k}\cdot\boldsymbol{a}_1} & 0 \end{pmatrix}, \tag{3}$$

where t_1 is the intralayer hopping parameter. Reformulating the 2×2 effective Hamiltonian matrix with the Pauli matrices [41,56,59], we obtain

$$H_{\text{eff}}(\boldsymbol{k}) = d_x(\boldsymbol{k})\sigma_x + d_y(\boldsymbol{k})\sigma_y. \tag{4}$$

Based on Eq. (4), we deduce the $d_x(\boldsymbol{k})$ and $d_y(\boldsymbol{k})$ terms, which are expanded into

$$d_x(\boldsymbol{k}) = -t_1 - t_1\cos[\boldsymbol{k}\cdot(\boldsymbol{a}_1 - \boldsymbol{a}_2)] - t_1\cos(\boldsymbol{k}\cdot\boldsymbol{a}_1), \tag{5}$$

$$d_y(\boldsymbol{k}) = -t_1\sin[\boldsymbol{k}\cdot(\boldsymbol{a}_1 - \boldsymbol{a}_2)] - t_1\sin(\boldsymbol{k}\cdot\boldsymbol{a}_1). \tag{6}$$

Consequently, we have the eigenvalues of the Hamiltonian $E_\pm = \pm\sqrt{d_x^2(\boldsymbol{k}) + d_y^2(\boldsymbol{k})}$. When $d_x(\boldsymbol{k}) = d_y(\boldsymbol{k}) = 0$, a pair of the Dirac points occur at the K point $\frac{\boldsymbol{b}_1-\boldsymbol{b}_2}{3}$ and the K' point $\frac{\boldsymbol{b}_2-\boldsymbol{b}_1}{3}$ of the Brillouin zone.

When we consider the 3D lattice by stacking 2D hexagonal lattices, the translation vectors are changed into

$$\boldsymbol{a}_1 = \frac{a}{2}(1, \sqrt{3}, 0),\quad \boldsymbol{a}_2 = \frac{a}{2}(-1, \sqrt{3}, 0),\quad \boldsymbol{a}_3 = d(0, 0, 1), \tag{7}$$

where d is the out-of-plane lattice constant. Similarly, the corresponding reciprocal lattice vectors are listed as follows:

$$\boldsymbol{b}_1 = \frac{2\pi}{a}\left(1, \frac{\sqrt{3}}{3}, 0\right),\quad \boldsymbol{b}_2 = \frac{2\pi}{a}\left(-1, \frac{\sqrt{3}}{3}, 0\right),\quad \boldsymbol{b}_3 = \frac{2\pi}{d}(0, 0, 1). \tag{8}$$

Taking into account the introduced $\boldsymbol{a}_3$ vectors, the effective Hamiltonian for the 3D case can be written in the form

$$H_{\text{eff}}(\boldsymbol{k}) = \begin{pmatrix} 0 & -t_1 - t_1 e^{i\boldsymbol{k}\cdot(\boldsymbol{a}_2-\boldsymbol{a}_1)} - t_1 e^{-i\boldsymbol{k}\cdot\boldsymbol{a}_1} - t_2 e^{i\boldsymbol{k}\cdot(\boldsymbol{a}_3-\boldsymbol{a}_1)} \\ -t_1 - t_1 e^{i\boldsymbol{k}\cdot(\boldsymbol{a}_1-\boldsymbol{a}_2)} - t_1 e^{i\boldsymbol{k}\cdot\boldsymbol{a}_1} - t_2 e^{i\boldsymbol{k}\cdot(\boldsymbol{a}_1-\boldsymbol{a}_3)} & 0 \end{pmatrix}, \tag{9}$$

where t_2 is the interlayer hopping parameter.

For the 3D case, the effective Hamiltonian with the Pauli matrices remains

$$H_{\text{eff}}(\boldsymbol{k}) = d_x(\boldsymbol{k})\sigma_x + d_y(\boldsymbol{k})\sigma_y. \tag{10}$$

Similarly, we arrive at the $d_x(\boldsymbol{k})$ and $d_y(\boldsymbol{k})$ terms, and expand them into

$$d_x(\boldsymbol{k}) = -t_1 - t_1\cos[\boldsymbol{k}\cdot(\boldsymbol{a}_1 - \boldsymbol{a}_2)] - t_1\cos(\boldsymbol{k}\cdot\boldsymbol{a}_1) - t_2\cos[\boldsymbol{k}\cdot(\boldsymbol{a}_1 - \boldsymbol{a}_3)], \tag{11}$$

$$d_y(\boldsymbol{k}) = -t_1\sin[\boldsymbol{k}\cdot(\boldsymbol{a}_1 - \boldsymbol{a}_2)] - t_1\sin(\boldsymbol{k}\cdot\boldsymbol{a}_1) - t_2\sin[\boldsymbol{k}\cdot(\boldsymbol{a}_1 - \boldsymbol{a}_3)]. \tag{12}$$

The appearance of band-crossing points requires $d_x(\boldsymbol{k}) = d_y(\boldsymbol{k}) = 0$, where the number of arguments (k_x, k_y, k_z) in Eq. (10) is greater than the number of functions, *viz.*, $d_x(\boldsymbol{k}) = 0$ and $d_y(\boldsymbol{k}) = 0$. Therefore, one can get infinite solutions for $\boldsymbol{k}$ that satisfy the two functions and form a continuous nodal ring in the Brillouin zone. When the inversion symmetry of the 3D sonic crystal is broken, an additional $d_z(\boldsymbol{k})\sigma_z$ term is introduced into the Hamiltonian [56]:

$$H_{\text{eff}}(\boldsymbol{k}) = d_x(\boldsymbol{k})\sigma_x + d_y(\boldsymbol{k})\sigma_y + d_z(\boldsymbol{k})\sigma_z. \tag{13}$$

Considering the hopping strengths and on-site energies, the tight-binding Hamiltonian is expressed as

$$H_{\text{eff}}(\boldsymbol{k}) = \begin{pmatrix} \frac{c_A-c_B}{2} + (t_A - t_B)(1 - \cos(\boldsymbol{k}\cdot\boldsymbol{a}_3)) & -t_1 - t_1 e^{i\boldsymbol{k}\cdot(\boldsymbol{a}_2-\boldsymbol{a}_1)} - t_1 e^{-i\boldsymbol{k}\cdot\boldsymbol{a}_1} - t_2 e^{i\boldsymbol{k}\cdot(\boldsymbol{a}_3-\boldsymbol{a}_1)} \\ -t_1 - t_1 e^{i\boldsymbol{k}\cdot(\boldsymbol{a}_1-\boldsymbol{a}_2)} - t_1 e^{i\boldsymbol{k}\cdot\boldsymbol{a}_1} - t_2 e^{i\boldsymbol{k}\cdot(\boldsymbol{a}_1-\boldsymbol{a}_3)} & \frac{c_B-c_A}{2} + (t_B - t_A)(1 - \cos(\boldsymbol{k}\cdot\boldsymbol{a}_3)) \end{pmatrix}, \tag{14}$$

where t_A and t_B represent the interlayer hopping strengths between A-A sites and B-B sites. c_A and c_B are the on-site energies at A and B sites, respectively. We further derive

$$d_z(\boldsymbol{k}) = \frac{c_A - c_B}{2} + (t_A - t_B)(1 - \cos(\boldsymbol{k}\cdot\boldsymbol{a}_3)), \qquad (15)$$

with $d_x(\boldsymbol{k})$ and $d_y(\boldsymbol{k})$ in Eqs. (11) and (12) unchanged. In this case, the existence of band-crossing points requires $d_x(\boldsymbol{k}) = d_y(\boldsymbol{k}) = d_z(\boldsymbol{k}) = 0$, where the number of arguments equals the number of functions. As a result, one will get discrete solutions for $\boldsymbol{k}$ that satisfy the functions and form the Weyl points in the Brillouin zone.

In regard to the surface states, the 3D sonic crystal can be viewed as an arrangement of a series of dimerized chains, resembling the Su-Schrieffer-Heeger (SSH) model [39,41,56]. The inversion symmetry in the proposed system guarantees the Zak phase quantized, where the Zak phase only possesses the values 0 and π that correspond to the trivial and nontrivial Zak phases, respectively [60]. To demonstrate this point, we calculate the Zak phase of the one-dimensional (1D) system parametrized with the in-plane momentum (k_x, k_y). With the denotation of $k_\parallel = (k_x, k_y)$, we define the Zak phase along k_z direction as $\theta_{k_\parallel} = \int A_{k_\parallel} dk_\perp$, where $A_{k_\parallel} = \langle u_{n,\boldsymbol{k}} | i\partial_{k_z} | u_{n,\boldsymbol{k}} \rangle$ is the Berry connection, with $u_n(\boldsymbol{k})$ the normalized eigenfunction of a Bloch mode in the nth band and $\boldsymbol{k}$ the reduced wave number of the mode. Finally, we confirm that the Zak phase along the k_z direction equals to π for $k_\parallel$ outside the nodal ring, whereas it is zero for $k_\parallel$ inside the nodal ring [41,54].

III. TOPOLOGICAL NODAL LINE STATES

A. Drumhead surface states

In this section, we start from the projected band structure of a perfect supercell slab that is periodic in the x-y plane and truncated in the z direction with 30 unit cells. Figure 4(a) shows the profile of nodal surface dispersion in the k_x-k_y momentum space. The degenerate dispersions appear outside the projected nodal ring. In Fig. 4(a), the surface Brillouin zone is divided into two regions with trivial and nontrivial Zak phases by the projection of the nodal ring. The blue region outside the projection of the nodal line has the nontrivial π Zak phase, while the gray region inside the nodal line projection has a trivial Zak phase of 0. The nontrivial Zak phase is the topological invariant behind the nodal surface band. To show the band feature, we calculate the projected band structure on the (001) surface at $k_y = 0$, as shown in Fig. 4(b). The gray lines denote the projected bulk bands. The degenerate blue lines are the nodal surface dispersions, which span from 451 to 503 Hz. In order to check the eigenfield distribution of the surface modes, we choose two eigenstates 1 and 2, as marked by the circles in Fig. 4(b). Figure 4(c) shows that the nodal surface states are well confined at the truncated surface and render a field polarization with the sound pressure distributed in only one sublattice. When we alter the size of sphere cavities on the surface, the nodal surface bands could become nearly dispersionless with a large density of states outside the projected nodal ring, in analogy to the vibration of a drum surface [49,53], which is also termed as drumhead surface dispersion. In the calculation, the radius of sphere cavities on the surface is 1.29 cm, different from the radius of sphere cavities in the bulk 1.5 cm. The sphere cavities with size modulation can be viewed as effective defects, which contributes to the correction of the on-site energy near the surface [41]. Figure 5(a) shows the profile of drumhead

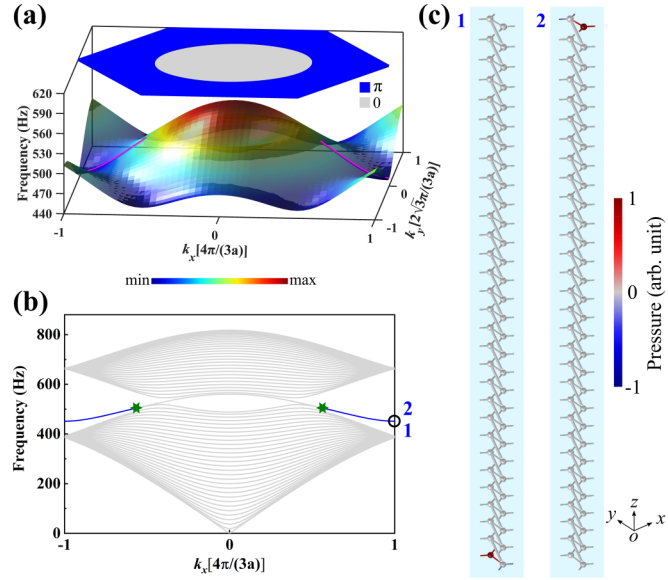

FIG. 4. (a) The nodal surface bands from the band-structure calculation of a perfect supercell slab. Upper panel: The Zak phase distribution. (b) The projected band structure at $k_y = 0$. The nodal line dispersions are denoted by the blue lines. The green stars represent the band-crossing points. (c) Pressure-field distributions of the eigenmodes at 1, 2 points marked by black circles in (b).

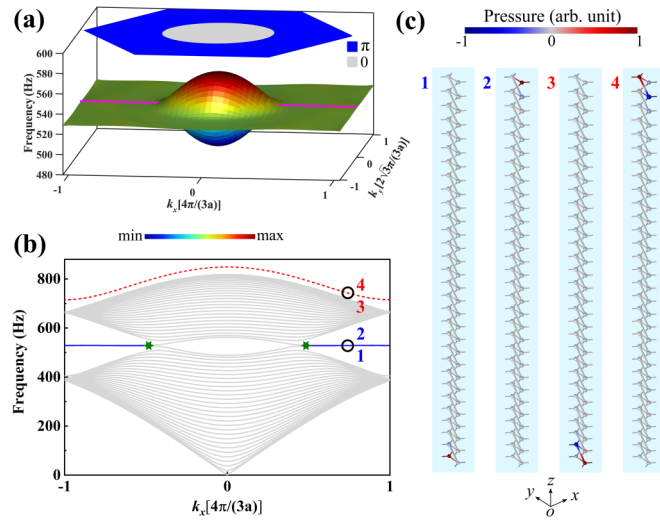

FIG. 5. (a) The drumhead surface-state bands. A drumhead profile is formed by calculating the band structure of a supercell slab with the surface cavities fine-tuned. Upper panel: The Zak phase distribution. (b) The projected band structure at $k_y = 0$. The drumhead surface states and the Tamm-like surface states at higher frequencies are denoted by the blue and red lines. The green stars are the band-crossing points. (c) Pressure-field distributions of the eigenmodes at 1, 2, 3, 4 points marked by the black circles in (b). The pressure fields are normalized by the maximum. The frequency of drumhead surface states is 529 Hz.

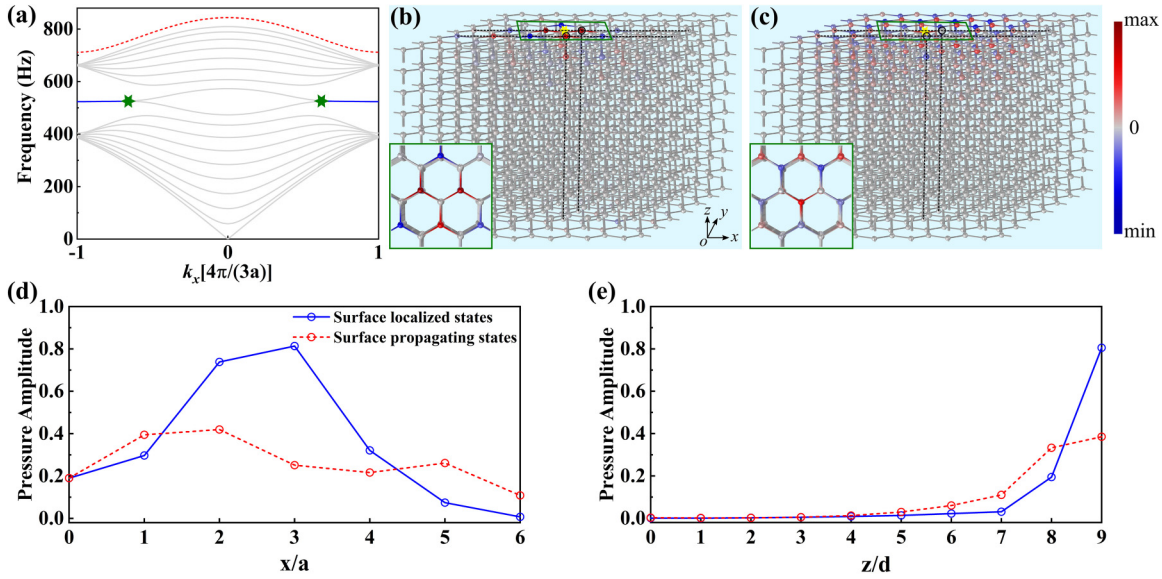

FIG. 6. (a) The projected band structure of a supercell slab at $k_y = 0$. The supercell consists of ten unit cells along the z direction. The drumhead modes appear nearby 523 Hz (blue lines). (b) Pressure distribution in a 3D lattice ($7 \times 7 \times 10$ unit cells) at 523 Hz. The yellow star labels the source position. The zoom-in inset exhibits distinct sublattice polarization, where the pressure field locates in one sublattice. (c) Pressure distribution in the 3D lattice at 826 Hz. The zoom-in inset shows no sublattice polarization. (d) Pressure amplitudes of surface states along the dashed lines in the x direction for the cases of (b) and (c). (e) Pressure amplitudes of surface states along the dashed lines in the z direction for the cases of (b) and (c).

surface dispersion in the k_x–k_y momentum space of a dressed supercell slab. The projected band structure on the (001) surface at $k_y = 0$ is shown in Fig. 5(b). The degenerate blue solid lines denote the nearly flat drumhead surface dispersions, with the frequencies spanning from 528.3 to 529 Hz. Noticeably, drumhead surface states have no overlap with bulk bands, which indicates that the flat surface states can be exclusively excited. Since the size of sphere cavities on the surface is altered, the Tamm-like surface states will emerge, as denoted by the red lines at higher frequencies in Fig. 5(b). Here, the drumhead surface states stem from the projection of nodal lines on the (001) surface, which are topologically nontrivial with a strong energy localization on the surface. The Tamm-like surface states are topologically trivial, since they arise from the surface defects [61]. Since drumhead surface states possess vanishing group velocities, it is expected that there exists a strong localization of sound due to the large density of states. We optionally choose four eigenstates 1, 2, 3, and 4, as marked by the circles in Fig. 5(b). The results show that the surface states are well confined at the truncated surface and decay exponentially into the bulk, as shown in Fig. 5(c). Except for the field polarization, the drumhead surface states 1 and 2 render a stronger energy localization on the surface due to the nontrivial π Zak phase, similar to the end states in 1D SSH models.

B. Excitation of surface states

For simplicity, we employ a reduced model with ten layers along the z direction to investigate the properties of surface states. Figure 6(a) shows the projected band structure of the supercell slab. Due to the finite-size effect of the supercell, dispersion curves are redshifted in the spectrum. For example, in Fig. 6(a), the drumhead surface states span from 523.2 to 526.6 Hz (<530 Hz in Fig. 2), while the high-frequency surface dispersions span from 712 to 844 Hz. The pointlike source excitation is imposed in a 3D sonic crystal with the dimensions of $7 \times 7 \times 10$ unit cells, without using a particular wave form or a fixed momentum. We conduct full-wave simulations in the pressure acoustic module of the commercial finite-element solver COMSOL MULTIPHYSICS. The top and bottom surfaces are rigid, while side surfaces are perfectly matched with absorbers. In Fig. 6(b), a monopole source, denoted by a yellow star, is placed on the top surface at the operation frequency of 523 Hz. The pressure-field distribution indicates that acoustic waves are not only localized on the top surface but also have little penetration normal to the surface, which benefits from the large density of drumhead states. Note that the operation wavelength $\lambda \approx 3.8a$, where a, as aforementioned, is the in-plane lattice constant. Therefore, the 3D sound trapping is a bulk property instead of the local resonance of sphere cavities. Figure 6(c) shows the pressure-field distribution of high-frequency surface states at 826 Hz with a nontrivial group velocity in reference to Fig. 6(a). Note that a clear sublattice polarization can also be observed in the present model. As shown in the insets of Figs. 6(b) and 6(c), the pressure field of drumhead surface states is distributed in one sublattice, while the pressure field of Tamm-like surface states resides in both sublattices. Quantitative analyses are displayed in Figs. 6(d) and 6(e), which describe the pressure-amplitude distributions along the dashed lines as marked in Figs. 6(b) and 6(c). The result in Fig. 6(d) reveals that high-frequency surface states in the x-y plane manifest no field localization in comparison with the drumhead states. From Fig. 6(e), we also find that in the direction normal to the surface (z axis), drumhead states are more

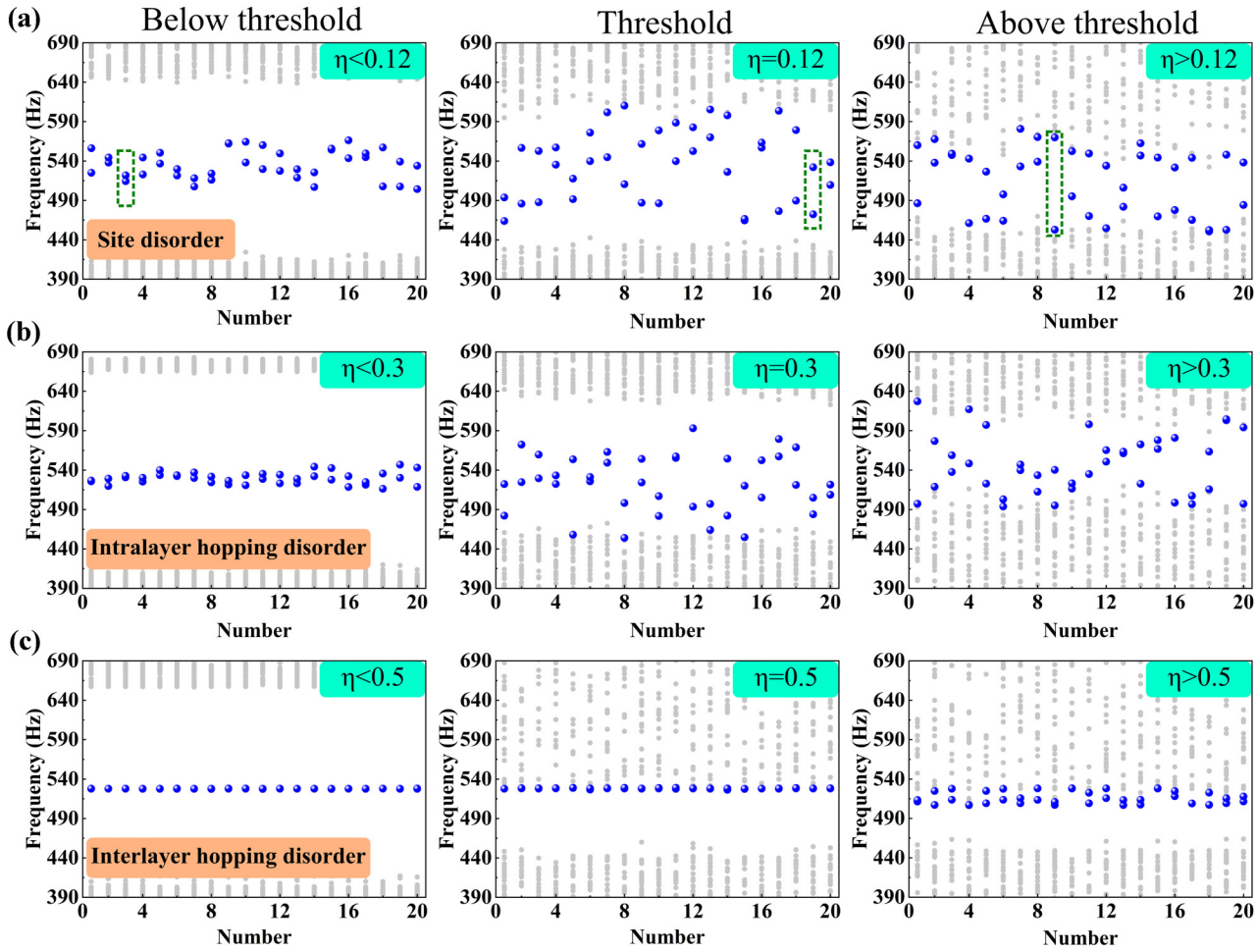

FIG. 7. (a) The band-structure evolution in the presence of site disorders with different strengths. (b) The band-structure evolution in the presence of intralayer hopping disorders with different strengths. (c) The band-structure evolution in the presence of interlayer hopping disorders with different strengths. The disorder strengths are set to be below, at, and above the threshold for each case.

confined than the high-frequency surface states with a larger Q factor.

C. Robustness of surface states

Protected by the inherent topology (nontrivial topological invariant), the drumhead surface states are supposed to be robust against structural disorders. In this section, a uniform random function is employed to set the structural parameters via the finite-element solver COMSOL MULTIPHYSICS 5.3$^{\text{tm}}$ linked with MATLAB. In the calculation, the supercell slab satisfies the Floquet periodic conditions along the x and y directions, with the random disorders taken within a certain range around the exact values and introduced along the z direction. This simplified approach is also adopted in previous work [41]. The 3D ball-and-stick sonic crystal can be regarded as comprising three basic elements, *viz.*, sphere cavities, in-plane connecting channels, and out-of-plane connecting channels. Therefore, we impose three types of disorders (site disorders, intralayer hopping disorders, and interlayer hopping disorders) to test the robustness of drumhead surface states against the disorder strength. In Fig. 7, we calculate the band structure of the supercell slab with 30 unit cells in the z direction in the presence of disorders. We first study the influence of site disorders by varying the radii of all lattice cavities, as shown in Fig. 7(a). Here η is employed to represent the strength of disorders, where the radii of cavities are uniformly taken in the range from $(1-\eta)r_S$ to $(1+\eta)r_S$. For the selected strength of disorders, we calculate the band structure for 20 times with different randomly distributed disorders in the z direction, to obtain the distribution trends of surface modes in the band gap, where the modes at $k_x = 4\pi/(3a)$ and $k_y = 0$ are chosen for demonstration. When the strength of site disorders is small ($\eta = 0.05$), we can distinguish the surface modes (blue spheres) from the bulk modes (gray dots) in the band structure, as shown by the left panel of Fig. 7(a). As the strength of site disorders is enhanced to a certain value [$\eta = 0.12$, the middle panel of Fig. 7(a)], the surface modes begin to merge with the bulk modes, which can be regarded as the threshold. Over the threshold, for example $\eta = 0.25$, more surface modes are mixing with the bulk modes, as shown by the right panel of Fig. 7(a). Figures 7(b) and 7(c) present influences of intralayer hopping disorders and interlayer hopping disorders by varying the cross sections of in-plane and out-of-plane channels. The results show the thresholds for these two cases locate at $\eta = 0.3$ and $\eta = 0.5$,

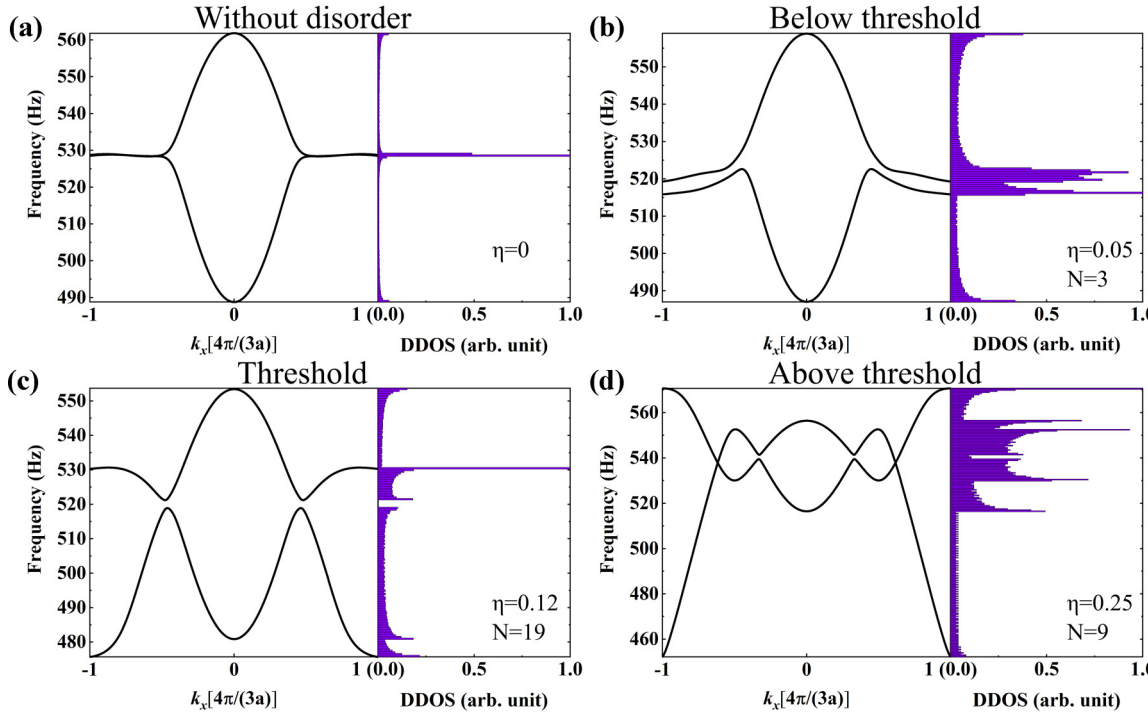

FIG. 8. The evolution of drumhead surface bands and the associated DDOS via the structural disorders. (a) The case without structural disorders ($\eta = 0$). (b) The case of site disorders below threshold ($\eta = 0.05$, $N = 3$). (c) The case of site disorders at the threshold ($\eta = 0.12$, $N = 19$). (d) The case of site disorders above threshold ($\eta = 0.25$, $N = 9$). The cases in (b)–(d) correspond to the selected ones marked by the dashed boxes in Fig. 7(a).

respectively. It is worth nothing that the drumhead surface states are more robust against the hopping disorders than the site disorders. The reasons lie in the fact that the site disorders will cause a nontrivial $d_z(\boldsymbol{k})\sigma_z$ term in the Hamiltonian, which makes the nodal ring gap out. However, the hopping disorders by changing coupling strengths t_1 and t_2 lead to the alterations of $d_x(\boldsymbol{k})\sigma_x$ and $d_y(\boldsymbol{k})\sigma_y$ in the Hamiltonian [41], with the $d_z(\boldsymbol{k})\sigma_z$ term trivial. Therefore, the nodal ring and drumhead surface states are robust against the hopping disorders.

We also show the evolution of drumhead bands and the associated directional density of states (DDOS) via the structural disorders, for example, the site disorders with different strengths as shown in Fig. 8. Here the DDOS at a certain frequency f_0 describes the number of modes inside an interval $[f_0, f_0 + \Delta f]$ [62]. In our case, the equivalent frequency interval is set at $\Delta f = 0.5$ Hz and the DDOS is normalized with the maximum. For comparison, we firstly show the band structure and DDOS of drumhead surface bands in the absence of disorders in Fig. 8(a). Obviously, the nearly dispersionless dispersions correspond to a very large DDOS featured with a distinctive sharp peak at the degenerate frequencies. When we introduce site disorders of weak strength below threshold into the lattice, for example, $\eta = 0.05$ and $N = 3$ in Fig. 8(b), the drumhead bands are distorted and all degeneracies are lifted. However, the DDOS is still localized in the central region of the frequency range ($515.7 \sim 522.7$ Hz). As the strength of site disorders is enhanced to reach the threshold, the bands are repelled to form a band gap with DDOS being zero, as shown in Fig. 8(c). Above the threshold, Fig. 8(d) shows that the bands are merging together again to form trivial bulk bands, where DDOS is not localized in the frequency range of interest.

To verify the robustness of drumhead surface states against disorders, we present the pressure-field distributions in the whole 3D sonic crystal with dimensions of $7 \times 7 \times 10$ unit cells in the presence of site disorders, intralayer hopping disorders, and interlayer hopping disorders, respectively. Figure 9(a) shows the field distribution of bulk states at 350 Hz, as a comparison to characterize the degree of field localization. Figures 9(b)–9(d) present the field distributions of surface states in the 3D lattices with those three types of disorders at the strength $\eta = 0.05$, which shows that the drumhead states are robust against weak-strength disorders. To quantitatively investigate these disorder effects, we extract the pressure amplitudes along the x and z directions, as shown by the dashed lines in Figs. 9(a)–9(d), and plot them in Figs. 9(e) and 9(f), respectively. From Figs. 9(e) and 9(f), we find out that different from the bulk states that are obviously extended into the interior region, the surface states are much more localized on the top surface even on the existence of site and hopping disorders.

In addition, we study the influence of the number of disorders on the robustness of nodal-ring states via band-structure evolution. As an example, we impose interlayer hopping disorders to test the robustness of drumhead states against the number of disorders. In Fig. 10, we calculate the band structure of the supercell slab with 30 unit cells in the z direction in the presence of disorders at $k_x = 4\pi/(3a)$ and $k_y = 0$. The strength of interlayer hopping disorders is $\eta = 0.6$, which is above the threshold for the bulk disorder case in Fig. 7(c). In the supercell slab, the interlayer hopping

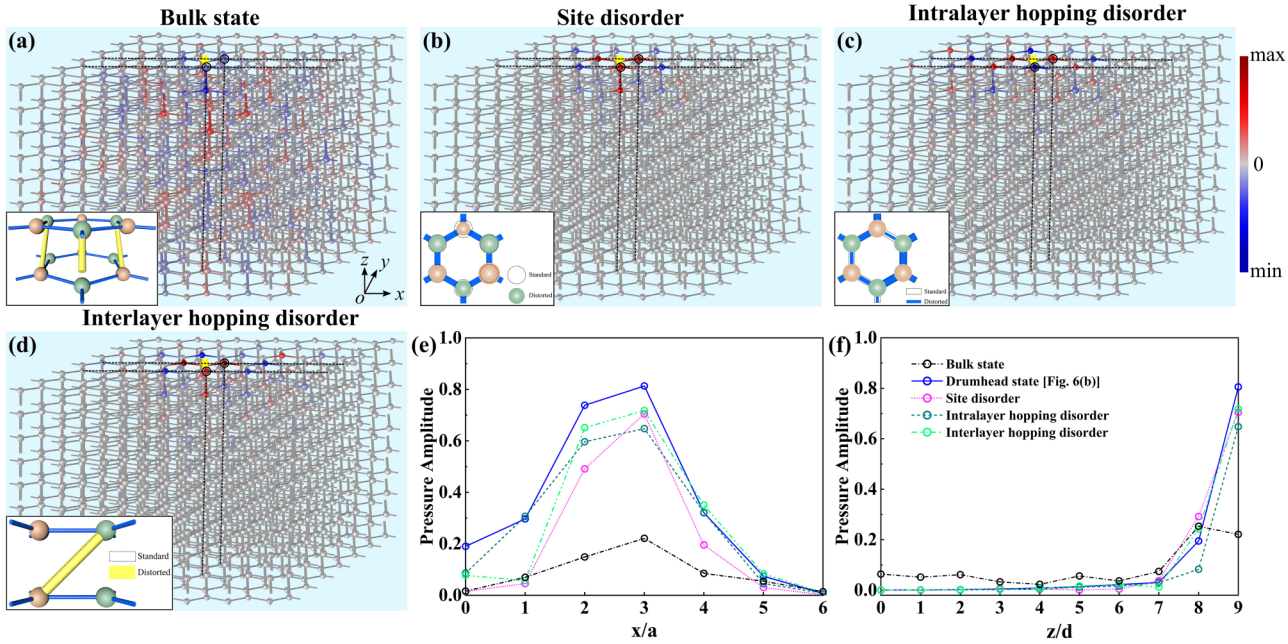

FIG. 9. (a) Pressure distribution of bulk states in the 3D lattice ($7 \times 7 \times 10$ unit cells) at 350 Hz. (b) Pressure distribution of surface states in the 3D lattice with site disorders. The operation frequency is 505 Hz. (c) Pressure distribution in the 3D lattice with intralayer hopping disorders. (d) Pressure distribution in the 3D lattice with interlayer hopping disorders. The operation frequency in (c) and (d) is 523 Hz. We excite the surface states by using a pointlike source with the pressure amplitude 1 Pa. (e) Pressure amplitudes along the x direction in the cases of (a)–(d) and Fig. 6(b). (f) Pressure amplitudes along the z direction in the cases of (a)–(d) and Fig. 6(b).

disorders are introduced from outside layers to the interior ones. In the left panel of Fig. 10, when the disorders are imposed in the two surface layers, the surface states are stable in the band structure. As the distributed disorders expand to the outside six layers (the middle panel of Fig. 10), the surface states begin to merge with bulk states, which can be regarded as a threshold. Above the threshold, for example, the outside 18 layers disturbed by disorders, more surface states are mixing with bulk states, as shown in the right panel of Fig. 10. The results show that the number of strong-strength disorders can change the robustness of drumhead states.

D. Intrinsic and nonintrinsic excitation

In the end, we explore the pressure-field distributions at intrinsic and nonintrinsic excitations, namely the sources positioned on the surface and in the bulk, respectively. Here we focus on a thicker 3D sonic crystal with the dimensions of $7 \times 7 \times 30$ unit cells. Since the finite-size effect is much suppressed, the frequency of drumhead surface states is 529 Hz, very close to the degeneracy frequency of nodal lines in Fig. 2 (530 Hz). We first study the intrinsic excitation with the sound source at 529 Hz placed on the top surface, as shown in Fig. 11(a). The result shows the formation of drumhead states that are well localized on the top surface in terms of the flat surface dispersions and nontrivial topological property (π Zak phase). For comparison, we also show the case of nonintrinsic excitation in Fig. 11(b), where the source at 529 Hz is inserted into the bulk. In this case, the source cannot excite the drumhead states but operate in the band-gap region of the lattice. Therefore, sound waves from the

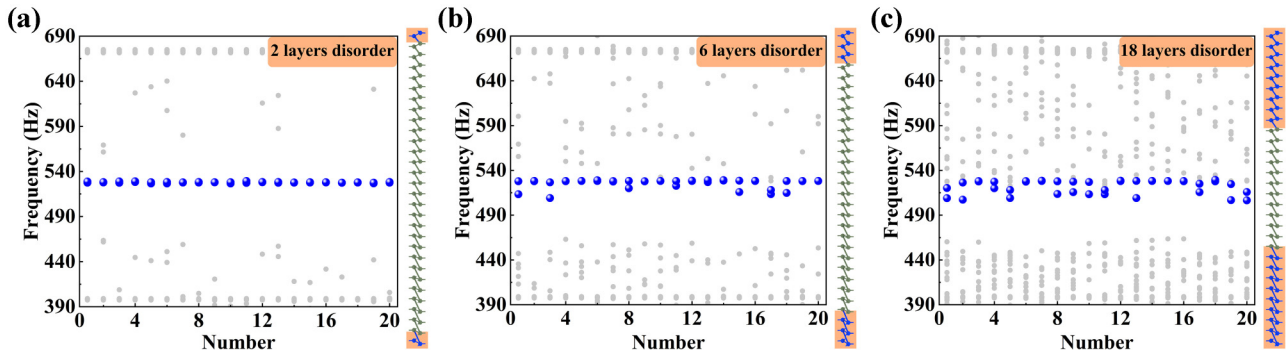

FIG. 10. The band-structure evolution in the presence of interlayer hopping disorders. The disorders are imposed in (a) the 2 surface layers, (b) the outside 6 layers, and (c) the outside 18 layers. The strength of interlayer hopping disorders is $\eta = 0.6$. The schematics show the distribution of disorders.

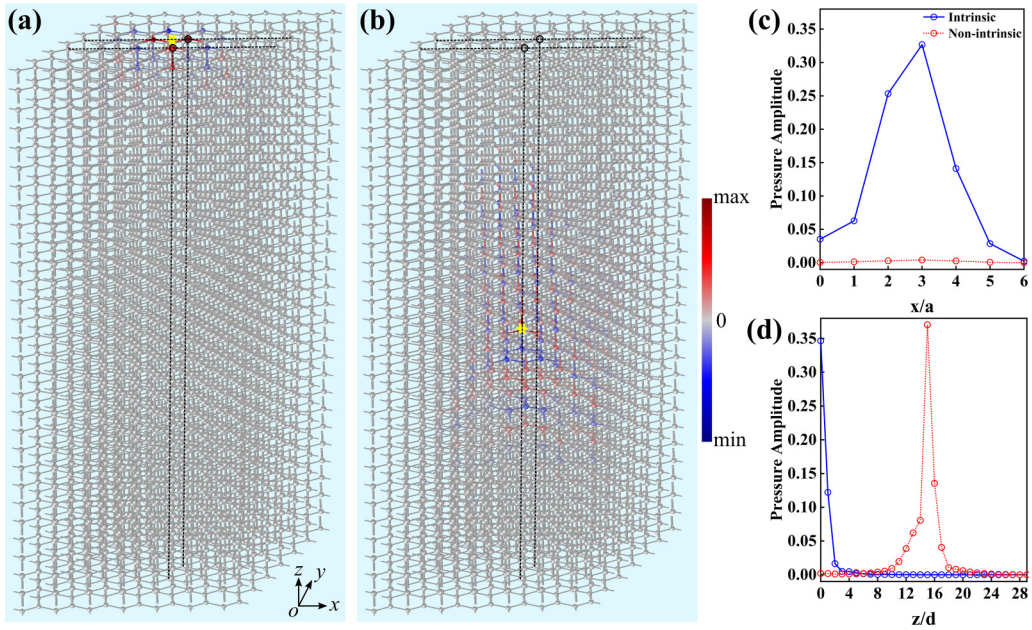

FIG. 11. (a) Pressure distribution for the intrinsic excitation on the surface of the 3D lattice ($7 \times 7 \times 30$ unit cells) at 529 Hz. (b) Pressure distribution for the nonintrinsic excitation in the bulk. In (a) and (b), the yellow star marks the source position. (c) Pressure amplitudes along the x direction (dashed lines) in (a) and (b). (d) Pressure amplitudes along the z direction (dashed lines) in (a) and (b). Here we use a pointlike sound source with the pressure amplitude 1 Pa for the intrinsic and nonintrinsic excitations.

source are completely reflected by the 3D periodic structure due to absolute band gaps of the sonic crystal. Quantitative studies are shown in Figs. 11(c) and 11(d), where the pressure amplitudes along the dashed lines in Figs. 11(a) and 11(b) are plotted. Evidently, the pressure fields are localized on the surface for the intrinsic excitation and trapped in the bulk for the nonintrinsic excitation.

IV. CONCLUSION

To summarize, we present a scheme for the implementation of topological nodal line states in 3D ball-and-stick sonic crystals that are protected by the time-reversal and inversion symmetries. We show that a closed nodal ring is formed in the 3D momentum space on condition that the interlayer coupling strength is above a threshold (>the in-plane coupling strength). Outside the projection of the nodal ring on the (001) surface of the Brillouin zone, we find the existence of flat drumhead surface states with the nontrivial Zak phase of π. A tight-binding model is proposed to illustrate the nodal lines and flat drumhead surface states. The drumhead states are featured with strong field localization on the surface with sublattice polarization, which is robust even on various imperfect conditions, such as site disorders, intralayer hopping disorders, and interlayer hopping disorders. Based on the evolution of supercell band structures and DDOS, we demonstrate the robustness of drumhead states against weak-strength disorder strengths and the number of surface defects/disorders, respectively. This intriguing property can be further exploited for versatile applications of sound trapping or frequency filtering. Our findings may also advance the current knowledge of topological acoustics and enrich the nodal line physics in 3D sonic crystals.

ACKNOWLEDGMENTS

This work was supported by the National Key Research and Development Program of China (Grants No. 2017YFA0303402 and No. 2017YFA0304700), National Natural Science Foundation of China (Grants No. 11674119, No. 11674077, No. 11690030, and No. 11690032). X.-F.Z. acknowledges the financial support from the Bird Nest Plan of HUST and the Fundamental Research Funds for the Central Universities (Grant No. 2019kfyRCPY136).

[1] M. Z. Hasan and C. L. Kane, Rev. Mod. Phys. **82**, 3045 (2010).
[2] N. P. Armitage, E. J. Mele, and A. Vishwanath, Rev. Mod. Phys. **90**, 015001 (2018).
[3] K. v. Klitzing, G. Dorda, and M. Pepper, Phys. Rev. Lett. **45**, 494 (1980).
[4] F. D. M. Haldane, Phys. Rev. Lett. **61**, 2015 (1988).
[5] C. L. Kane and E. J. Mele, Phys. Rev. Lett. **95**, 226801 (2005).
[6] C. L. Kane and E. J. Mele, Phys. Rev. Lett. **95**, 146802 (2005).
[7] X. Zhang, M. Xiao, Y. Cheng, M. H. Lu, and J. Christensen, Commun. Phys. **1**, 97 (2018).
[8] G. Ma, M. Xiao, and C. T. Chan, Nat. Rev. Phys. **1**, 281 (2019).
[9] Z. Yang, F. Gao, X. Shi, X. Lin, Z. Gao, Y. Chong, and B. Zhang, Phys. Rev. Lett. **114**, 114301 (2015).
[10] X. Ni, C. He, X. C. Sun, X.-p. Liu, M. H. Lu, L. Feng, and Y. F. Chen, New J. Phys. **17**, 053016 (2015).

[11] A. B. Khanikaev, R. Fleury, S. H. Mousavi, and A. Alu, Nat. Commun. **6**, 8260 (2015).
[12] Y. Ding, Y. Peng, Y. Zhu, X. Fan, J. Yang, B. Liang, X. Zhu, X. Wan, and J. Cheng, Phys. Rev. Lett. **122**, 014302 (2019).
[13] L. H. Wu and X. Hu, Phys. Rev. Lett. **114**, 223901 (2015).
[14] C. He, X. Ni, H. Ge, X. C. Sun, Y. B. Chen, M. H. Lu, X. P. Liu, and Y. F. Chen, Nat. Phys. **12**, 1124 (2016).
[15] Y. G. Peng, C. Z. Qin, D. G. Zhao, Y. X. Shen, X. Y. Xu, M. Bao, H. Jia, and X. F. Zhu, Nat. Commun. **7**, 13368 (2016).
[16] S. Y. Yu, C. He, Z. Wang, F. K. Liu, X. C. Sun, Z. Li, H. Z. Lu, M. H. Lu, X. P. Liu, and Y. F. Chen, Nat. Commun. **9**, 3072 (2018).
[17] M.-J. Tuo, L.-H. Zhang, D. Liu, R.-W. Peng, R.-H. Fan, Z.-G. Chen, Y. Wu, D.-X. Qi, and M. Wang, Phys. Rev. B **99**, 205432 (2019).
[18] J. Lu, C. Qiu, M. Ke, and Z. Liu, Phys. Rev. Lett. **116**, 093901 (2016).
[19] J. Lu, C. Qiu, L. Ye, X. Fan, M. Ke, F. Zhang, and Z. Liu, Nat. Phys. **13**, 369 (2017).
[20] X. Wu, Y. Meng, J. Tian, Y. Huang, H. Xiang, D. Han, and W. Wen, Nat. Commun. **8**, 1304 (2017).
[21] Z. G. Geng, Y. G. Peng, Y. X. Shen, D. G. Zhao, and X. F. Zhu, Appl. Phys. Lett. **113**, 033503 (2018).
[22] A. A. Burkov, M. D. Hook, and L. Balents, Phys. Rev. B **84**, 235126 (2011).
[23] X. Wan, A. M. Turner, A. Vishwanath, and S. Y. Savrasov, Phys. Rev. B **83**, 205101 (2011).
[24] Z. Wang, Y. Sun, X.-Q. Chen, C. Franchini, G. Xu, H. Weng, X. Dai, and Z. Fang, Phys. Rev. B **85**, 195320 (2012).
[25] Z. K. Liu, B. Zhou, Y. Zhang, Z. J. Wang, H. M. Weng, D. Prabhakaran, S.-K. Mo, Z. X. Shen, Z. Fang, X. Dai, Z. Hussain, and Y. L. Chen, Science **343**, 864 (2014).
[26] H. Weng, C. Fang, Z. Fang, B. A. Bernevig, and X. Dai, Phys. Rev. X **5**, 011029 (2015).
[27] G. Chang, S. Y. Xu, X. Zhou, S. M. Huang, B. Singh, B. Wang, I. Belopolski, J. Yin, S. Zhang, A. Bansil, H. Lin, and M. Z. Hasan, Phys. Rev. Lett. **119**, 156401 (2017).
[28] Z. Yan, R. Bi, H. Shen, L. Lu, S.-C. Zhang, and Z. Wang, Phys. Rev. B **96**, 041103(R) (2017).
[29] L. Lu, L. Fu, J. D. Joannopoulos, and M. Soljačić, Nat. Photonics **7**, 294 (2013).
[30] L. Lu, Z. Wang, D. Ye, L. Ran, L. Fu, J. D. Joannopoulos, and M. Soljačić, Science **349**, 622 (2015).
[31] J. Noh, S. Huang, D. Leykam, Y. D. Chong, K. P. Chen, and M. C. Rechtsman, Nat. Phys. **13**, 611 (2017).
[32] Q. Yan, R. Liu, Z. Yan, B. Liu, H. Chen, Z. Wang, and L. Lu, Nat. Phys. **14**, 461 (2018).
[33] W. Gao, B. Yang, B. Tremain, H. Liu, Q. Guo, L. Xia, A. P. Hibbins, and S. Zhang, Nat. Commun. **9**, 950 (2018).
[34] L. Xia, Q. Guo, B. Yang, J. Han, C. X. Liu, W. Zhang, and S. Zhang, Phys. Rev. Lett. **122**, 103903 (2019).
[35] M. Kim, D. Lee, D. Lee, and J. Rho, Phys. Rev. B **99**, 235423 (2019).
[36] M. Xiao, W.-J. Chen, W.-Y. He, and C. T. Chan, Nat. Phys. **11**, 920 (2015).
[37] F. Li, X. Huang, J. Lu, J. Ma, and Z. Liu, Nat. Phys. **14**, 30 (2017).
[38] H. Ge, X. Ni, Y. Tian, S. K. Gupta, M. H. Lu, X. Lin, W. D. Huang, C. T. Chan, and Y. F. Chen, Phys. Rev. Appl. **10**, 014017 (2018).
[39] Z. Xiong, H. X. Wang, H. Ge, J. Shi, J. Luo, Y. Lai, M. H. Lu, and J. H. Jiang, Phys. Rev. B **97**, 180101(R) (2018).
[40] M. Xiao, X.-Q. Sun, and S. Fan, Phys. Rev. B **99**, 094206 (2019).
[41] W. Deng, J. Lu, F. Li, X. Huang, M. Yan, J. Ma, and Z. Liu, Nat. Commun. **10**, 1769 (2019).
[42] H. Qiu, C. Qiu, R. Yu, M. Xiao, H. He, L. Ye, M. Ke, and Z. Liu, Phys. Rev. B **100**, 041303(R) (2019).
[43] A. Merkel and J. Christensen, arXiv:1906.06204.
[44] Y. Yang, H.-x. Sun, J.-p. Xia, H. Xue, Z. Gao, Y. Ge, D. Jia, S.-q. Yuan, Y. Chong, and B. Zhang, Nat. Phys. **15**, 645 (2019).
[45] B. Xie, H. Liu, H. Cheng, Z. Liu, S. Chen, and J. Tian, Phys. Rev. Lett. **122**, 104302 (2019).
[46] C. He, S. Y. Yu, H. Wang, H. Ge, J. Ruan, H. Zhang, M. H. Lu, and Y. F. Chen, Phys. Rev. Lett. **123**, 195503 (2019).
[47] Y. Yang, J.-p. Xia, H.-x. Sun, Y. Ge, D. Jia, S.-q. Yuan, S. A. Yang, Y. Chong, and B. Zhang, Nat. Commun. **10**, 5185 (2019).
[48] H. He, C. Qiu, X. Cai, M. Xiao, M. Ke, F. Zhang, and Z. Liu, arXiv:1911.00806.
[49] S.-Y. Yang, H. Yang, E. Derunova, S. S. P. Parkin, B. Yan, and M. N. Ali, Adv. Phys.: X **3**, 1414631 (2018).
[50] C.-K. Chiu and A. P. Schnyder, Phys. Rev. B **90**, 205136 (2014).
[51] R. Yu, Q. Wu, Z. Fang, and H. Weng, Phys. Rev. Lett. **119**, 036401 (2017).
[52] Y. Kim, B. J. Wieder, C. L. Kane, and A. M. Rappe, Phys. Rev. Lett. **115**, 036806 (2015).
[53] H. Weng, Y. Liang, Q. Xu, R. Yu, Z. Fang, X. Dai, and Y. Kawazoe, Phys. Rev. B **92**, 045108 (2015).
[54] J. Zhao, R. Yu, H. Weng, and Z. Fang, Phys. Rev. B **94**, 195104 (2016).
[55] Q. Xu, R. Yu, Z. Fang, X. Dai, and H. Weng, Phys. Rev. B **95**, 045136 (2017).
[56] K. Luo, R. Yu, and H. Weng, Research **2018**, 6793752 (2018).
[57] Q.-F. Liang, J. Zhou, R. Yu, Z. Wang, and H. Weng, Phys. Rev. B **93**, 085427 (2016).
[58] A. H. Castro Neto, F. Guinea, N. M. R. Peres, K. S. Novoselov, and A. K. Geim, Rev. Mod. Phys. **81**, 109 (2009).
[59] K. Luo, J. Feng, Y. X. Zhao, and R. Yu, arXiv:1810.09231.
[60] J. Zak, Phys. Rev. Lett. **62**, 2747 (1989).
[61] Y. Plotnik, M. C. Rechtsman, D. Song, M. Heinrich, J. M. Zeuner, S. Nolte, Y. Lumer, N. Malkova, J. Xu, A. Szameit, Z. Chen, and M. Segev, Nat. Mater. **13**, 57 (2014).
[62] M. Ke, Z. He, S. Peng, Z. Liu, J. Shi, W. Wen, and P. Sheng, Phys. Rev. Lett. **99**, 044301 (2007).